IEEE Open Journal of the
Communications Society

Received 2 March 2022; accepted 24 March 2022. Date of publication 30 March 2022; date of current version 8 April 2022.

Digital Object Identifier 10.1109/OJCOMS.2022.3163574

Ambient Backscatter Assisted Co-Existence in Aerial-IRS Wireless Networks

SOURABH SOLANKI [1] (Member, IEEE), SUMIT GAUTAM [2] (Member, IEEE),
SHREE KRISHNA SHARMA [1] (Senior Member, IEEE),
AND SYMEON CHATZINOTAS [1] (Senior Member, IEEE)

[1] Interdisciplinary Center for Security, Reliability and Trust (SnT), University of Luxembourg, 1855 Luxembourg City, Luxembourg

[2] Department of Electrical Engineering, Indian Institute of Technology—Indore, Indore 453552, India

CORRESPONDING AUTHOR: S. SOLANKI (e-mail: sourabh.solanki@uni.lu)

This work was supported in part by the Luxembourg National Research Fund (FNR)-5G-Sky Project under Grant FNR/C19/IS/13713801/5G-Sky, and in part by SMC funded Micro5G Project. A preliminary version of this paper has been submitted to IEEE VTC2022-Spring.

ABSTRACT Ambient backscatter communication (AmBC) is an emerging technology that has the potential to offer spectral- and energy-efficient solutions for the next generation wireless communications networks, especially for the Internet of Things (IoT). Intelligent reflecting surfaces (IRSs) are also perceived to be an integral part of the beyond 5G systems to complement the traditional relaying scheme. To this end, this paper proposes a novel system design that enables the co-existence of a backscattering secondary system with the legacy primary system. This co-existence is primarily driven by leveraging the AmBC technique in IRS-assisted unmanned aerial vehicle (UAV) networks. More specifically, an aerial-IRS mounted on a UAV is considered to be employed for cooperatively relaying the transmitted signal from a terrestrial primary source node to a user equipment on the ground. Meanwhile, capitalizing on the AmBC technology, a backscatter capable terrestrial secondary node transmits its information to a terrestrial secondary receiver by modulating and backscattering the ambient relayed radio frequency signals from the UAV-IRS. We comprehensively analyze the performance of the proposed design framework with co-existing systems by deriving the outage probability and ergodic spectral efficiency expressions. Moreover, we also investigate the asymptotic behavior of outage performance in high transmit power regimes for both primary and secondary systems. Importantly, we analyze the performance of the primary system by considering two different scenarios, i.e., optimal phase shifts design and random phase shifting at IRS. Finally, based on the analytical performance assessment, we present numerical results to provide various useful insights and also provide simulation results to corroborate the derived theoretical results.

INDEX TERMS Ambient backscatter communication (AmBC), intelligent reflecting surface (IRS), unmanned aerial vehicle (UAV), performance analysis, relaying.

I. INTRODUCTION

INTELLIGENT reflecting surfaces (IRSs) are envisaged to have a great potential for their applications in the next generation of wireless networks, including the Internet-of-Things (IoT). The IRSs are comprised of a synthetic array having sub-wavelength passive reflector elements that can adjust the phase shifts of the impinging waves to efficiently steer them towards the destination which in turn can enhance the communication performance. In the context of the future 6G wireless networks, the IRSs can offer higher energy- and spectral- efficiencies with reduced hardware complexity and cost compared to the traditional cooperative relaying schemes [1], [2]. On the other hand, unmanned aerial vehicles (UAVs) are believed to play a crucial role in providing wider wireless connectivity and coverage to the ground users [3], [4]. Due to their mobility and high altitude, UAVs can establish their individual direct line-of-sight (LoS) links with the ground users to counteract blockages and shadowing in the complex urban environment [5].

As such, several efforts have been made to integrate the IRS with UAV to form aerial-IRS networks [6]–[12]. Aerial-IRSs are particularly suitable for small lightweight UAVs which can support limited payloads and, therefore, may not be able to carry heavy radio-frequency (RF) transceivers like the ones deployed at the base stations (BSs) or relays [6]. In addition, it has been observed that the propulsion energy is the major source of energy consumption for UAV, and energy required for communication is negligible compared to it. Increasing payload can significantly reduce the flight time of UAV [5]. Therefore, reducing the payload seems to be one of the possible solutions to improve the flight time of UAVs. To this end, deploying active nodes (e.g., BSs/relays) would consume a lot of energy that can eventually limit the endurance and operational life-time of the UAVs. Thus, employing a passive IRS on the UAVs can save some energy cost. Furthermore, in comparison to the IRS deployed on buildings, aerial-IRS enjoys more flexibility as it can establish the desired line-of-sight (LoS) links and avoid a large power loss. In this context, the authors in [7] proposed a reinforcement learning based approach to enhance the performance of millimeter wave (mmWave) networks using aerial IRS. In [8], the performance of an integrated UAV-IRS relaying system has been analyzed in terms of outage probability, ergodic capacity, and energy efficiency for three different transmission modes. Lu *et al.* considered an aerial-IRS enabled relaying method to assist the BS for an extended coverage [9]. It aimed at maximizing the worst case signal-to-noise ratio (SNR) in a targeted area. Further, the authors in [10] considered the application of an aerial-IRS for the anti-jamming communications. The study in [11] investigates the application of UAV-IRS for IoT networks to improve the coverage, reliability, and spectral efficiency. In [12], the placement of aerial-IRS has been optimized to assist the downlink transmission from a high-altitude platform (HAP).

On another front, ambient backscatter communication (AmBC) is an evolving technology that can utilize the RF signals from the ambient BSs, TV towers, or access points, for the transmission without requiring active RF components [13], [14]. Communication using AmBC does not require dedicated spectrum and thus, offers spectral efficient means for wireless information transmission. Leveraging on the potential of AmBC, various research works have recently focused on this technology [15]–[23]. For instance, the authors in [15] introduced a spectrum sharing paradigm for IoT devices based on AmBC. Authors in [16] studied a cognitive backscatter network based spectrum sharing for passive IoT. A symbiotic radio cooperative AmBC has been analyzed in [17] to facilitate the spectrum sharing. The authors in [18] examined the outage performance in three different paradigms of cooperative AmBC systems. In addition, a few other works have explored the design of IRS-based AmBC networks. A work in [19] considered an IRS-aided backscattering system to realize the reliable communication for IoT applications. In [20], IRS and AmBC have been utilized to enhance the performance in symbiotic radio system. To enhance the backscattering links, IRS has been utilized for non-orthogonal multiple access (NOMA) assisted backscatter communication system in [21]. The authors in [22] integrated IRS, AmBC, and wireless powered technologies to support the device-to-device communication. In [23], a deep reinforcement learning is considered for optimization in IRS-assisted AmBC system. More recently, the authors in [24] have proposed the synergy between AmBC and IRSs by showing that certain functionalities such as medium access control can be outsourced to the programmable wireless environments to simplify the hardware of the AmBC device.

Motivated by the above-mentioned discussion, this paper proposes a novel system design to investigate the potential of combining the IRS, UAV, and AmBC technologies.[1] Specifically, the proposed design considers the application of a cooperative aerial-IRS to help the information transmission from a terrestrial primary source node to its destination. Meanwhile, a secondary system co-exists on the same spectrum by relying on the AmBC assistance. The considered UAV-IRS methodology can provide a wide coverage in ultra-dense environments, whereas, the employment of AmBC augments in the effective usage of the spectral resources.

In contrast to the conventional cognitive radio based spectrum sharing [26], [27], the co-existence using AmBC primarily differs in two aspects. First, the secondary transmitter (Tag) does not generate its own RF signal, but rather exploits the RF signal of primary transmitter for its information transmission. Second, due to interference from the primary system, the secondary receiver (Reader) relies upon the successive interference cancellation (SIC) to decode its information. This spectrum sharing concept has also been referred to as a symbiotic radio or cognitive backscattering [20]. For such a system configuration, we comprehensively investigate its performance by deriving theoretical expressions for the outage probability (OP) and ergodic spectral efficiency (ESE). Furthermore, we also examine the asymptotic behavior of outage performance for primary and secondary systems in high transmit power regime. Based on our investigations, we provide various insights into the system design.

Notations: We use $\mathbb{E}[\cdot]$ to represent the expectation and $\mathcal{CN}(0, \sigma^2)$ to represent complex normal distribution having mean zero and variance σ^2. Also, $\mathbf{I}_N$ denotes the identity matrix of size $N \times N$, $K_v(\cdot)$ represents v-th order modified Bessel function of second kind [28, eq. (8.432.1)], $\mathrm{Ei}(\cdot)$ is an exponential integral function [28, eq. (8.21)], while $\mathcal{D}_{(\cdot)}(\cdot)$ denotes parabolic cylinder function [28, eq. (9.240)]. We also use $f_X(\cdot)$ and $F_X(\cdot)$ to denote the probability

---

[1] A part of this paper is reported in [25], where the performance is investigated over Rayleigh fading channels for the random phase shifting design at IRS.

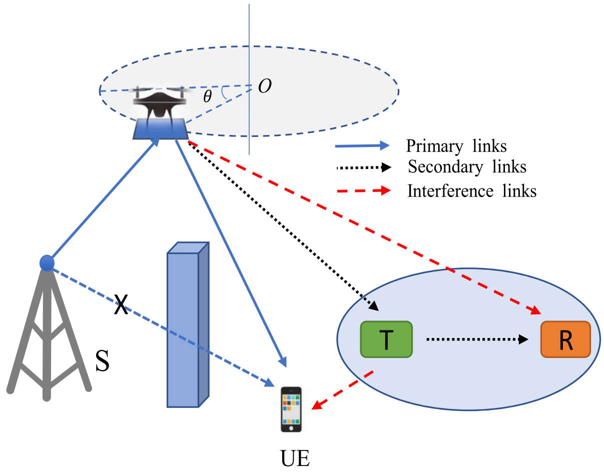

FIGURE 1. **System model of AmBC assisted UAV-IRS network.**

density function (PDF) and the cumulative distribution function (CDF) of a random variable (RV) X, respectively, and $\Pr[\,\cdot\,]$ to represent the probability. Finally, $\Upsilon(\cdot,\cdot)$, $\Gamma(\cdot,\cdot)$ and $\Gamma(\cdot)$ denote, respectively, the lower incomplete, the upper incomplete, and the complete gamma functions [28, eq. (8.350)] and $(\cdot)!$ represents factorial operation.

II. SYSTEM MODEL

As shown in the Fig. 1, we consider a wireless network comprising a primary system including a transmit node S, a UAV-IRS [8], and a UE on the ground. Secondary system includes a backscatter capable tag/transmitter T and a corresponding reader/receiver R. The notion of primary and secondary systems can be inferred as follows. In the considered setup, both primary as well as secondary users can be a part of the same network wherein one has high priority (i.e., legacy primary system) over the other (i.e., backscattering secondary system) and hence they transmit over the same spectral resources to improve the spectrum utilization efficiency.

In this framework, the primary system may be useful to offload the cell traffic using an aerial node to serve a cell-edge user which is beyond the strong coverage of a base station in a macrocell. Whereas, the secondary system can include IoT devices where T can be a sensor node and R an actuator. Usually, IoT devices require less power and generally have low-rate requirements. Owing to the battery-limitations, it is desirable to save the energy in any possible ways to prolong the operational time of the IoT devices. Leveraging the AmBC technology, an IoT node can transmit the signal without having to generate its own RF signal. Additionally, the secondary system can also include energy-limited device-to-device (D2D) communication where backscatter capable node T will be D2D transmitter and R will be a D2D receiver.

Further, the system operates at sub-6 GHz band [29]. Due to either an absent or blocked LoS link for direct transmission between S and UE, the S seeks assistance from a cooperative node to relay its information. Consequently, an aerial-IRS mounted on a UAV is considered to be deployed for relaying the information of S. Aerial-IRS is equipped with N passive reflective elements that can be reconfigured using a controller. For the secondary system, the backscattering capable node T receives the ambient RF signal from UAV-IRS and thereby modulates its own information for the passive transmission towards reader node R. The backscattering node T is considered to be a semi-passive device having an internal power source which can support the low-power circuit operations without requiring energy harvesting [17]. Hereby, we assume the cooperation between primary and secondary systems to facilitate the joint decoding at R which, in turn, can achieve a reliable backscatter communication [17], [18].

The locations of S, UAV-IRS, and the ground users are denoted by $\{\mathbf{q_b}, \mathbf{q_u}, \mathbf{q_k}\} \in \mathbb{R}^{3\times 1}$ with $\mathbf{k} \in \{\mathbf{e}, \mathbf{t}, \mathbf{r}\}$, respectively, in a three-dimensional plane. The UAV is assumed to be a fixed-wing type which follows a circular trajectory of radius r at a fixed altitude $H \in [H_{\min}, H_{\max}]$ with a constant velocity, where $H_{\min}$ and $H_{\max}$ represent the minimum and maximum possible altitudes, respectively. In general, for the stationary UE on the ground, the UAV can hover at a given location to serve the user at any particular time instant. To model the 3D movement of the UAV, let us consider θ as an angle of the UAV location with reference to x-axis at any given instant. Thus, UAV's location can be represented as $\mathbf{q_u} = [r\cos\theta \quad r\sin\theta \quad H]^T$ where θ governs the UAV movement in a circle of radius r at an altitude of H above the ground.

Hereby, we adopt a channel model for air-to-ground (A2G) propagation which accounts for both the large scale fading as well as small scale fading. More specifically, for the UAVs, the large scale fading model is dependent on the altitude, distance, and elevation angle which are dominant factors for A2G propagation. As such, the elevation angle between S and UAV, denoted as $\phi_{\mathbf{b},\mathbf{u}}$, and between ground users and UAV, denoted as $\phi_{\mathbf{k},\mathbf{u}}$, can be expressed as

$$\phi_{\mathbf{b},\mathbf{u}} = \arctan\left(\frac{H}{|\mathbf{q_u} - \mathbf{q_b}|}\right), \; \phi_{\mathbf{k},\mathbf{u}} = \arctan\left(\frac{H}{|\mathbf{q_u} - \mathbf{q_k}|}\right). \tag{1}$$

As UAV can flexibly establish the LoS with the terrestrial users, the LoS probability between UAV and ground nodes, i.e., S and UEs, is given by [30]

$$p^L(\phi_{\ell,\mathbf{u}}) = \frac{1}{1 + C\exp\big(-B(\phi_{\ell,\mathbf{u}} - C)\big)}, \quad \forall \ell \in \{\mathbf{b},\ \mathbf{k}\} \tag{2}$$

where B and C are environment dependent constants. The path-loss exponent is given by

$$\alpha(\phi_{\ell,\mathbf{u}}) = p^L(\phi_{\ell,\mathbf{u}})c_\ell + f_\ell, \tag{3}$$

where c_ℓ and f_ℓ are constants which depend on the uplink and downlink environment.

To characterize the small scale fading, all the channel coefficients are assumed to be independent RVs whose envelopes follow a Nakagami-m distribution [31], [32]. Let the channels from S to n-th IRS element at UAV, with $n \in \mathcal{N} \triangleq \{1, \dots, N\}$, and from n-th IRS element to UE and R, are denoted, respectively, as $h_{b,n} \sim Nak(m_{bu}, \Omega_{bu})$, $h_{n,e} \sim Nak(m_{ue}, \Omega_{ue})$, and $h_{n,r} \sim Nak(m_{ur}, \Omega_{ur})$. The composite channels [16]–[18] from n-th IRS element to R and UE via T are represented by $h_{n,t_r} \sim Nak(m_{ut_r}, \Omega_{ut_r})$ and $h_{n,t_e} \sim Nak(m_{ut_e}, \Omega_{ut_e})$, respectively.

Further, we can represent vectors of the channel coefficients as $\mathbf{h}_{b,u} = [h_{b,1}, \dots, h_{b,N}]^H$, $\mathbf{h}_{u,e} = [h_{1,e}, \dots, h_{N,e}]^H$, $\mathbf{h}_{u,r} = [h_{1,r}, \dots, h_{N,r}]^H$, $\mathbf{h}_{u,t_e} = [h_{1,t_e}, \dots, h_{N,t_e}]^H$, and $\mathbf{h}_{u,t_r} = [h_{1,t_r}, \dots, h_{N,t_r}]^H$. In addition, $\Theta = \mathrm{diag}(e^{j\varphi_1}, \dots, e^{j\varphi_n}, \dots, e^{j\varphi_N})$ is a phase shift matrix, where $\varphi_n \in [0, 2\pi), \forall n$, is the phase shift by the n-th element. Nakagami-m distribution is a versatile model which encapsulates variety of fading scenarios. For example, it can also be used to describe the Rician fading by setting its parameter m as $m = \left(1 - \left(\frac{K}{k+1}\right)^2\right)^{-1}$ [31], where K is a Rician factor.

III. MODELING OF IRS-AIDED UAV NETWORKS

This section presents the modeling of the proposed aerial-IRS based AmBC network. We first describe the signal model and eventually formulate the SNR of various communication links. Then, based on the obtained SNR, we derive the probability of successful SIC.

A. SNR FORMULATION

For the information transmission in the considered system framework, firstly, a terrestrial node S transmits its symbol x with $\mathbb{E}[x^2] = 1$ to UE using the cooperation from UAV-IRS. In the meantime, the secondary node T modulates its own information c with $\mathbb{E}[c^2] = 1$, on the received ambient RF signal from UAV-IRS, to transmit for its destination R. As a result, the signal received at UE can be given as

$$y_e = \sqrt{P_b \tilde{d}_1}\,\mathbf{h}_{b,u}^H \boldsymbol{\Theta} \mathbf{h}_{u,e} x + \sqrt{P_b \eta \tilde{d}_2}\,\mathbf{h}_{b,u}^H \boldsymbol{\Theta} \mathbf{h}_{u,t_e} x c + \nu_e, \quad (4)$$

where P_b is the transmit power at the S, $\tilde{d}_1 = (d_{bu}/d_0)^{-\alpha(\phi_{\mathbf{b,u}})}(d_{ue}/d_0)^{-\alpha(\phi_{\mathbf{u,e}})}$, $\tilde{d}_2 = (d_{bu}/d_0)^{-\alpha(\phi_{\mathbf{b,u}})}(d_{ut}/d_0)^{-\alpha(\phi_{\mathbf{u,t}})}(d_{te}/d_0)^{-\alpha_o}$, with d_0 being the reference distance and $d_{bu} = \sqrt{|\mathbf{q}_b - \mathbf{q}_u|^2 + H^2}$, $d_{ue} = \sqrt{|\mathbf{q_e} - \mathbf{q}_u|^2 + H^2}$, $d_{ut} = \sqrt{|\mathbf{q_t} - \mathbf{q}_u|^2 + H^2}$, and $d_{te} = |\mathbf{q_t} - \mathbf{q_e}|$, are the distances between S to UAV-IRS, UAV-IRS to UE, and T to UE, respectively. α_o is the path-loss exponent for the terrestrial links, $\eta \in [0, 1]$ is the backscatter efficiency of T, and $\nu_e \sim \mathcal{CN}(0, \sigma_e^2)$ is the additive white Gaussian noise (AWGN). In (4), the second term accounts for the interference from the backscattered secondary transmission. Based on the received signal in (4), the UE decodes its information using the following signal-to-interference-plus-noise ratio (SINR)

$$\Lambda_E^x = \frac{P_b \tilde{d}_1 \left|\mathbf{h}_{b,u}^H \boldsymbol{\Theta} \mathbf{h}_{u,e}\right|^2}{P_b \eta \tilde{d}_2 \left|\mathbf{h}_{b,u}^H \boldsymbol{\Theta} \mathbf{h}_{u,t_e}\right|^2 + \sigma_e^2}. \quad (5)$$

On the other hand, the signal received at R can be given by

$$y_r = \sqrt{P_b \eta \tilde{d}_3}\,\mathbf{h}_{b,u}^H \boldsymbol{\Theta} \mathbf{h}_{u,t_r} x c + \sqrt{P_b \tilde{d}_4}\,\mathbf{h}_{b,u}^H \boldsymbol{\Theta} \mathbf{h}_{u,r} x + \nu_r, \quad (6)$$

where $\tilde{d}_3 = (d_{bu}/d_0)^{-\alpha(\phi_{\mathbf{b,u}})}(d_{ut}/d_0)^{-\alpha(\phi_{\mathbf{u,t}})}(d_{tr}/d_0)^{-\alpha_o}$, $\tilde{d}_4 = (d_{bu}/d_0)^{-\alpha(\phi_{\mathbf{b,u}})}(d_{ur}/d_0)^{-\alpha(\phi_{\mathbf{u,r}})}$, with $d_{ur} = \sqrt{|\mathbf{q_r} - \mathbf{q}_u|^2 + H^2}$, and $d_{tr} = |\mathbf{q_t} - \mathbf{q_r}|$ being the distances between UAV-IRS to R, and T to R, respectively, and $\nu_r \sim \mathcal{CN}(0, \sigma_r^2)$ is the AWGN. As highlighted earlier, due to cooperation between primary and secondary systems, node R can decode its information c using SIC [16]–[18]. Specifically, it first decodes the signal of UE while treating c as an interference and subsequently obtains its information by eliminating the decoded signal. As such, the SINR at R to decode the x can be given by

$$\Lambda_R^x = \frac{P_b \tilde{d}_4 \left|\mathbf{h}_{b,u}^H \boldsymbol{\Theta} \mathbf{h}_{u,r}\right|^2}{P_b \eta \tilde{d}_3 \left|\mathbf{h}_{b,u}^H \boldsymbol{\Theta} \mathbf{h}_{u,t_r}\right|^2 + \sigma_r^2}. \quad (7)$$

After eliminating the decoded signal x from its observation, R retrieves its information using the SNR[2]

$$\Lambda_R^c = \frac{P_b}{\sigma_r^2} \eta \tilde{d}_3 \left|\mathbf{h}_{b,u}^H \boldsymbol{\Theta} \mathbf{h}_{u,t_r}\right|^2. \quad (8)$$

Hereafter, it is assumed that the channel state information (CSI) of the pertinent channels are available at the S which can be feedback to IRS controller from a dedicated control channel [33]. Various methods of the channel estimation have been reported in existing works, for instance, see [34], [35]. Also, note that as IRS configures itself to optimize the phase shifts for UE, nodes T and R will experience the arbitrary phase shifts. For notational simplicity, let us represent the RVs $X = \mathbf{h}_{b,u}^H \boldsymbol{\Theta} \mathbf{h}_{u,e}$, $W = \mathbf{h}_{b,u}^H \boldsymbol{\Theta} \mathbf{h}_{u,t_e}$, $Y = \mathbf{h}_{b,u}^H \boldsymbol{\Theta} \mathbf{h}_{u,r}$, and $Z = \mathbf{h}_{b,u}^H \boldsymbol{\Theta} \mathbf{h}_{u,t_r}$.

Next, we derive the probability of successful SIC at R which determines the acceptable information transmission between secondary nodes T and R.

B. PROBABILITY OF SUCCESSFUL SIC

Recalling that reader node R first needs to decode the received signal from the legacy primary transmission for carrying out the SIC. Basically, the SIC capable receiver at R first decodes the stronger signal from the S and then subtract it from the combined received signal in (6) to finally extract its own information. We can define this requirement for node R as the condition of successful SIC. Mathematically, it is

---

[2] To mitigate the effect of triple fading at R, UAV's location can be optimized to maximize its SNR. However, this study is beyond the scope of the current work and is hence left for the future research.

the probability that the SINR Λ_R^x in (7) exceeds a predefined decoding threshold which can be expressed as

$$\begin{aligned} P_{sic}(\tau) &= \Pr\left[\Lambda_R^x > \tau\right] \\ &= 1 - \Pr\left[\frac{P_b \tilde{d}_4 \left|\mathbf{h}_{b,u}^H \boldsymbol{\Theta} \mathbf{h}_{u,r}\right|^2}{P_b \eta \tilde{d}_3 \left|\mathbf{h}_{b,u}^H \boldsymbol{\Theta} \mathbf{h}_{u,t_r}\right|^2 + \sigma_r^2} \leq \tau\right] \\ &= 1 - \int_{z=0}^{\infty} F_{|Y|^2}\left(\frac{\tau}{P_b \tilde{d}_4}\left(P_b \eta \tilde{d}_3 z + \sigma_r^2\right)\right) f_{|Z|^2}(z) dz, \end{aligned} \tag{9}$$

where τ is the minimum required threshold to decode the primary's signal. In the following theorem, we provide the closed-form solution of (9) to obtain the probability of successful SIC.

Theorem 1: The probability of successful SIC at R is given by

$$\begin{aligned} P_{sic}(\tau) = {} & \frac{1}{N\Omega_{bu}\Omega_{ut_r}} \exp\left(\frac{-\tau\sigma_r^2}{P_b \tilde{d}_4 N \Omega_{bu} \Omega_{ur}}\right) \\ & \times \left(\frac{\tilde{d}_4 N \Omega_{bu} \Omega_{ur} \Omega_{ut_r}}{\tau \eta \tilde{d}_3 \Omega_{ut_r} + \tilde{d}_4 \Omega_{ur}}\right). \end{aligned} \tag{10}$$

Proof: Please refer to Appendix A. ■

The result of Theorem 1 will be utilized to analyze the performance of backscattering secondary system in the subsequent section.

IV. PERFORMANCE ANALYSIS OF THE PROPOSED AMBC ASSISTED CO-EXISTENCE

This section analyzes the performance of the considered framework by evaluating two key metrics, e.g., OP and ESE.

A. OUTAGE PROBABILITY

Under this subsection, we compute the OPs for both legacy primary system and backscattering secondary system by deriving their analytical expressions. For the primary system, we consider two different scenarios viz., optimal phase shifts design and random phase shifting at IRS. To simplify the expressions and better understand them, we also derive the asymptotic behavior of OPs.

1) PRIMARY SYSTEM WITH OPTIMAL PHASE SHIFTS

The primary system is said to be in outage if the received SINR Λ_E^x at UE falls below a certain threshold. As such, for a given target rate $\mathcal{R}_p$, OP can be expressed as

$$P_{out}^{pri}(\mathcal{R}_p) = \Pr\left[\frac{P_b \tilde{d}_1 \left|\mathbf{h}_{b,u}^H \boldsymbol{\Theta} \mathbf{h}_{u,e}\right|^2}{P_b \eta \tilde{d}_2 \left|\mathbf{h}_{b,u}^H \boldsymbol{\Theta} \mathbf{h}_{u,t_e}\right|^2 + \sigma_e^2} \leq r_{th}^p\right], \tag{11}$$

where $r_{th}^p = 2^{\mathcal{R}_p} - 1$ is a threshold. Hereby, we consider a coherent phase shift design [36] to enhance the performance of primary user UE. In other words, it is assumed that the phase shifts from the IRS elements are adjusted in such a way that the reflected signals are co-phased, i.e., $\varphi_n = -\angle h_{b,n} h_{n,e}$ where $\angle x$ indicates the phase of a complex number x. Consequently, we can re-write the OP expression in (11) as

$$P_{out}^{pri}(\mathcal{R}_p) = \Pr\left[\frac{P_b \tilde{d}_1 \left(\sum_{n=1}^{N} |h_{b,n}||h_{n,e}|\right)^2}{P_b \eta \tilde{d}_2 \left|\mathbf{h}_{b,u}^H \boldsymbol{\Theta} \mathbf{h}_{u,t_e}\right|^2 + \sigma_e^2} \leq r_{th}^p\right]. \tag{12}$$

In the following theorem, we provide the analytical expression for the OP.

Theorem 2: The OP of primary system with optimal phase shifts is given by[3]

$$\begin{aligned} P_{out}^{pri}(\mathcal{R}_p) = {} & \sum_{n=0}^{L} \exp\left(\frac{\sigma_e^2}{P_b N \Omega_{bu} \Omega_{ut_e} \eta \tilde{d}_2}\right) \frac{2}{\Gamma(k_x + n + 1)} \\ & \times \mathcal{A}(\mathcal{R}_p) \frac{1}{N\Omega_{bu}\Omega_{ut_e}} \frac{\tilde{d}_1 \beta_x^2}{r_{th}^p \eta \tilde{d}_2}, \end{aligned} \tag{13}$$

with

$$k_x = N \frac{(\mathbb{E}[\Xi_n])^2}{\mathrm{Var}[\Xi_n]} \text{ and } \beta_x = \frac{\mathrm{Var}[\Xi_n]}{\mathbb{E}[\Xi_n]}. \tag{14}$$

Proof: Please refer to Appendix B. ■

To further obtain the insights into the derived OP expression, we obtain its asymptotic approximation at high transmit power, i.e., $P_b \to \infty$.

Corollary 1: The asymptotic OP of the primary system can be derived as

$$\begin{aligned} P_{out}^{pri}(\mathcal{R}_p) \underset{P_b \to \infty}{\simeq} & \sum_{n=0}^{L} \left(\frac{2\tilde{d}_1 \beta_x^2}{r_{th}^p \eta \tilde{d}_2 N \Omega_{bu} \Omega_{ut_e}}\right)^{-\frac{k_x+n}{2}} \\ & \times (k_x + n + 1) \exp\left(\frac{r_{th}^p \eta \tilde{d}_2 N \Omega_{bu} \Omega_{ut_e}}{8\tilde{d}_1 \beta_x^2}\right) \\ & \times \mathcal{D}_{-(k_x+n+2)}\left(\sqrt{\frac{r_{th}^p \eta \tilde{d}_2 N \Omega_{bu} \Omega_{ut_e}}{2\tilde{d}_1 \beta_x^2}}\right). \end{aligned} \tag{15}$$

Proof: See Appendix C. ■

Remark: It can be noted from (15) in Corollary 1 that OP of the primary system at asymptotic limit is independent of the transmit power P_b. Such independence from the transmit power will lead to an error floor in the outage performance. This observation can also be validated via numerical results, as we shall observe later in Section V.

2) PRIMARY SYSTEM WITH RANDOM PHASE SHIFTS

When perfect CSI is not available at S, the phase shifts of IRS can not be optimally co-phased viz., $\varphi_n \neq -\angle h_{b,n} h_{n,e}$. As a result, the UE will experience random phase shifts. As such, random phase shifting can avoid requisition of the global CSI and eventually reduce the system overhead. Random

---

[3] As in [8], we examine the performance for a given location of UAV. The average performance along the UAV trajectory can be numerically examined.

phase shifting may also be applicable for the scenarios when perfect CSI is not available due to various impairments. For this case, OP can be expressed as

$$P_{out,rp}^{pri}(\mathcal{R}_p) = \Pr\left[\frac{P_b\tilde{d}_1\left|\mathbf{h}_{b,u}^H\boldsymbol{\Theta}\mathbf{h}_{u,e}\right|^2}{P_b\eta\tilde{d}_2\left|\mathbf{h}_{b,u}^H\boldsymbol{\Theta}\mathbf{h}_{u,t_e}\right|^2+\sigma_e^2} \leq r_{th}^p\right]. \tag{16}$$

The following theorem provides the closed-form expression for the OP.

Theorem 3: The OP of primary system with random phase shifts can be expressed by

$$P_{out,rp}^{pri}(\mathcal{R}_p) = 1 - \frac{1}{N\Omega_{bu}\Omega_{ut_e}}\exp\left(\frac{-r_{th}^p\sigma_e^2}{P_b\tilde{d}_1N\Omega_{bu}\Omega_{ue}}\right) \times \left(\frac{r_{th}^p\eta\tilde{d}_2}{\tilde{d}_1N\Omega_{bu}\Omega_{ue}} + \frac{1}{N\Omega_{bu}\Omega_{ut_e}}\right)^{-1}. \tag{17}$$

Proof: Please refer to Appendix D. ■

Further, at asymptotic limit, i.e., $P_b \to \infty$, $P_{out,rp}^{pri}(\mathcal{R}_p)$ can be expressed as

$$P_{out,rp}^{pri}(\mathcal{R}_p) \underset{P_b\to\infty}{\simeq} 1 - \frac{\tilde{d}_1\Omega_{ue}}{\Omega_{ut_e}r_{th}^p\eta\tilde{d}_2 + \tilde{d}_1\Omega_{ue}}, \tag{18}$$

where (18) can be derived by computing the integral in (D.1) for $P_b \to \infty$.

Remark: Similar to the case of optimal phase shifts, OP of primary system with random phase shifting is also independent of the transmit power P_b at asymptotic limit which will give rise to an error floor. Moreover, it can also be noted that $P_{out,rp}^{pri}(\mathcal{R}_p)$ in (18) does not depend on number of reflecting elements N. Consequently, the outage performance may remain unaffected with respect to N at higher P_b. These inferences can also be verified using numerical results in Section V.

3) BACKSCATTERING SECONDARY SYSTEM

For the backscattering secondary system, an outage occurs if either R is unable to successfully perform SIC or SNR Λ_R^c at reader R falls below a specific threshold. Based on the SIC probability, the OP can be formulated as

$$P_{out}^{sec}(\mathcal{R}_s) = \bar{P}_{sic}(\tau) + P_{sic}(\tau)\Pr\left[\log_2\left(1+\Lambda_R^c\right) \leq \mathcal{R}_s\right], \tag{19}$$

where $P_{sic}(\tau)$ is as given in Theorem 1, with $\bar{P}_{sic}(\tau) = 1 - P_{sic}(\tau)$. On substituting the SNR Λ_R^c from (8), we rewrite (19) as

$$P_{out}^{sec}(\mathcal{R}_s) = \bar{P}_{sic}(\tau) + P_{sic}(\tau)\Pr\left[\frac{P_b}{\sigma_r^2}\eta\tilde{d}_3\left|\mathbf{h}_{b,u}^H\boldsymbol{\Theta}\mathbf{h}_{u,t_r}\right|^2 \leq r_{th}^s\right], \tag{20}$$

where $\mathcal{R}_s$ is a target rate and $r_{th}^s = 2^{\mathcal{R}_s} - 1$. Following corollary provides the closed-form solution for the above equation.

Corollary 2: The OP of the backscattering secondary system can be expressed as

$$P_{out}^{sec}(\mathcal{R}_s) = \bar{P}_{sic}(\tau) + P_{sic}(\tau) \times \sum_{k=0}^{1}(-1)^k\exp\left(\frac{-kr_{th}^s\sigma_r^2}{P_b\eta\tilde{d}_3N\Omega_{bu}\Omega_{ut_r}}\right). \tag{21}$$

Proof: Following the reasoning in Appendix A, it can be established that the RV $Z = \mathbf{h}_{b,u}^H\boldsymbol{\Theta}\mathbf{h}_{u,t_r}$ can be statistically characterized using a complex Gaussian distribution. Consequently, $|Z|^2$ will follow an exponential distribution with the CDF given by

$$F_{|Z|^2}(z) = 1 - \exp\left(-\frac{z}{N\Omega_{bu}\Omega_{ut_r}}\right). \tag{22}$$

Using this CDF in (21), we can obtain the desired expression in Corollary 2. ■

In the following corollary, we obtain asymptotic OP of the backscattering secondary system.

Corollary 3: At higher transmit power, i.e., $P_b \to \infty$, the asymptotic OP of the backscattering secondary system can be expressed as

$$P_{out}^{sec}(\mathcal{R}_s) \underset{P_b\to\infty}{\simeq} \bar{P}_{sic}^{asy}(\tau) + P_{sic}^{asy}(\tau)\frac{r_{th}^s\sigma_r^2}{P_b\eta\tilde{d}_3N\Omega_{bu}\Omega_{ut_r}}, \tag{23}$$

where $\bar{P}_{sic}^{asy}(\tau) = 1 - P_{sic}^{asy}(\tau)$ and $P_{sic}^{asy}(\tau)$ is given by

$$P_{sic}^{asy}(\tau) = \frac{\tilde{d}_4\Omega_{ur}}{\Omega_{ut_r}\tau\eta\tilde{d}_3+\tilde{d}_4\Omega_{ur}}. \tag{24}$$

Proof: See Appendix E. ■

Dependence of $P_{out}^{sec}(\mathcal{R}_s)$ on N at higher P_b signifies that the increase in the number of reflecting elements can enhance the OP performance of secondary. However, the product of P_b and N at their higher values leads to negligible second term in (23). As a result, the OP would be predominantly govern by the term $\bar{P}_{sic}^{asy}(\tau)$ and thus, saturated with respect to P_b and N owing to the independence from them.

Next, we analyze the ESE of the proposed network configuration for both primary and backscattering secondary systems.

B. ERGODIC SPECTRAL EFFICIENCY

In what follows under this subsection, we analyze another important performance metric called ESE for the legacy primary system as well as backscattering secondary system.

1) PRIMARY SYSTEM WITH OPTIMAL PHASE SHIFTS

Based on the SINR Λ_E^x in (5), the ESE for the primary system can be expressed as

$$C_{pri} = \mathbb{E}\left[\log_2\left(1 + \frac{P_b\tilde{d}_1\left|\mathbf{h}_{b,u}^H\boldsymbol{\Theta}\mathbf{h}_{u,e}\right|^2}{P_b\eta\tilde{d}_2\left|\mathbf{h}_{b,u}^H\boldsymbol{\Theta}\mathbf{h}_{u,t_e}\right|^2+\sigma_e^2}\right)\right]. \tag{25}$$

For the optimal phase shifts at IRS, (25) can be re-expressed as

$$
\begin{aligned}
C_{pri} &= \mathbb{E}\left[\log_2\left(1+\frac{P_b\tilde{d}_1\left(\sum_{n=1}^{N}|h_{b,n}||h_{n,e}|\right)^2}{P_b\eta\tilde{d}_2\left|\mathbf{h}_{b,u}^H\boldsymbol{\Theta}\mathbf{h}_{u,t_e}\right|^2+\sigma_e^2}\right)\right]\\
&= \mathbb{E}\left[\log_2\left(P_b\tilde{d}_1|\tilde{X}|^2+P_b\eta\tilde{d}_2|W|^2+\sigma_e^2\right)\right]\\
&\quad - \mathbb{E}\left[\log_2\left(P_b\eta\tilde{d}_2|W|^2+\sigma_e^2\right)\right] \qquad (26)
\end{aligned}
$$

where $\tilde{X} = \sum_{n=1}^{N}|h_{b,n}||h_{n,e}|$. It appears that obtaining the closed-form solution of the above expression is rather intricate. Therefore, we seek for its approximation by using the Jensen's inequality as follows

$$
\begin{aligned}
C_{pri} &\approx \log_2\left(P_b\tilde{d}_1\mathbb{E}\left[|\tilde{X}|^2\right]+P_b\eta\tilde{d}_2\mathbb{E}\left[|W|^2\right]+\sigma_e^2\right)\\
&\quad - \log_2\left(P_b\eta\tilde{d}_2\mathbb{E}\left[|W|^2\right]+\sigma_e^2\right), \qquad (27)
\end{aligned}
$$

following the statistical characterization, as derived in Appendix F, one can obtain

$$\mathbb{E}[|\tilde{X}|^2] = k_x\beta_x^2(1+k_x) \qquad (28)$$

$$\mathbb{E}[|W|^2] = N\Omega_{bu}\Omega_{ut_e}. \qquad (29)$$

Finally, using these values in (27), we can obtain a simplified approximation for the ESE of primary system with optimal phase shifts.

2) PRIMARY SYSTEM WITH RANDOM PHASE SHIFTS

The ESE for the primary system with random phase shifts at IRS can be given by

$$C_{pri,rp} = \mathbb{E}\left[\log_2\left(1+\frac{P_b\tilde{d}_1\left|\mathbf{h}_{b,u}^H\boldsymbol{\Theta}\mathbf{h}_{u,e}\right|^2}{P_b\eta\tilde{d}_2\left|\mathbf{h}_{b,u}^H\boldsymbol{\Theta}\mathbf{h}_{u,t_e}\right|^2+\sigma_e^2}\right)\right], \qquad (30)$$

which, on using the Jensen's inequality, can be expressed as

$$
\begin{aligned}
C_{pri} &\approx \log_2\left(P_b\tilde{d}_1\mathbb{E}\left[|X|^2\right]+P_b\eta\tilde{d}_2\mathbb{E}\left[|W|^2\right]+\sigma_e^2\right)\\
&\quad - \log_2\left(P_b\eta\tilde{d}_2\mathbb{E}\left[|W|^2\right]+\sigma_e^2\right). \qquad (31)
\end{aligned}
$$

Based on (D.2) in Appendix D, we can deduce that $\mathbb{E}[|X|^2] = N\Omega_{bu}\Omega_{ue}$. Using this along with (29) and thereby substituting them into (31), we can obtain the ESE of the primary system for the random phase shifts.

3) BACKSCATTERING SECONDARY SYSTEM

Depending on the SNR Λ_R^c in (8), the ESE for the secondary system can be formulated as

$$C_{sec} = P_{sic}(\tau)\mathbb{E}\left[\log_2\left(1+\frac{P_b}{\sigma_r^2}\eta\tilde{d}_3\left|\mathbf{h}_{b,u}^H\boldsymbol{\Theta}\mathbf{h}_{u,t_r}\right|^2\right)\right]. \qquad (32)$$

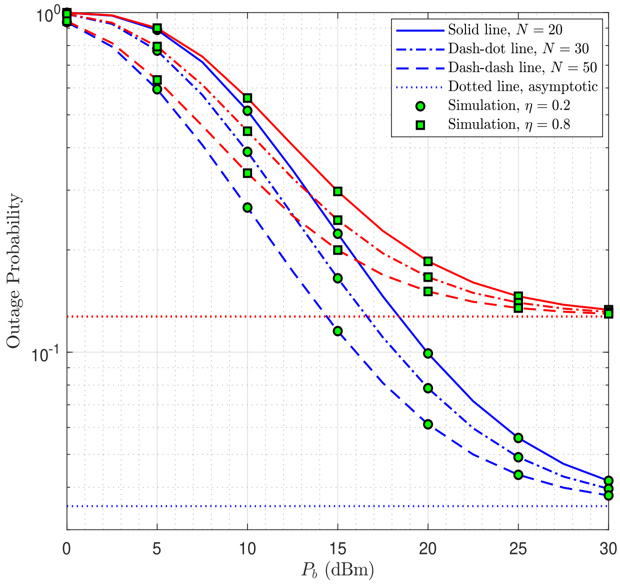

FIGURE 2. **OP of primary system with random phase shifts in terms of the transmit power P_b.**

On evaluating the above expectation, the exact closed-form expression for the ESE of backscattering secondary system can be given by

$$
\begin{aligned}
C_{sec} &= -\log_2(e)P_{sic}(\tau)\exp\left(\frac{\sigma_r^2}{P_b\eta\tilde{d}_3N\Omega_{bu}\Omega_{ut_r}}\right)\\
&\quad \times \mathrm{Ei}\left(\frac{-\sigma_r^2}{P_b\eta\tilde{d}_3N\Omega_{bu}\Omega_{ut_r}}\right). \qquad (33)
\end{aligned}
$$

The proof of the derivation of (33) is presented in Appendix G.

Based on the analyses in this section, the forthcoming section presents several numerical and simulation results to validate the theoretical analysis and thereby discusses the impact of various design parameters to provide insights.

V. NUMERICAL RESULTS AND DISCUSSION

This section presents the numerical results based on the theoretical analysis. Extensive Monte Carlo simulations have been performed to validate the derived analytical results. We set the several system parameters as $\Omega_{bu} = \Omega_{ur} = 2$, $\Omega_{ue} = 3.5$, $\Omega_{ut_e} = 0.1$, $\Omega_{ut_r} = 0.5$, $m_{bu} = m_{ue} = 1$, $C = 20$, $B = 0.5$, $c_\ell = -1.5$, $f_\ell = 3.5$ [30]. Without losing generality, we consider $H = 1.5$ km, $r = 0.5$ km, $R_p = 3$, $R_s = 0.1$, $d_0 = 1$ m, $\mathbf{q_b} = [-2 \;\; -2 \;\; 0]^T$ km, $\mathbf{q_e} = [3 \;\; 0 \;\; 0]^T$ km, $\mathbf{q_t} = [3 \;\; -1 \;\; 0]^T$ m, $\mathbf{q_r} = [5 \;\; -1 \;\; 0]^T$ m, $\alpha_o = 2.5$, $\tau = 0.1$, $\sigma_e^2 = \sigma_r^2 = -10$ dBm, unless stated otherwise. It is also assumed that, for the random phase shifts, the resulting phase errors are uniformly distributed between 0 and 2π. For illustrating the numerical results, we use solid/dash-dot/dash-dash lines to represent the analytical results derived in Section IV while dotted lines for the asymptotic results.

In Fig. 2, we plot the outage performance of primary network in terms of the transmit power P_b for the random phase shifts at IRS. Apparently, the analytical results

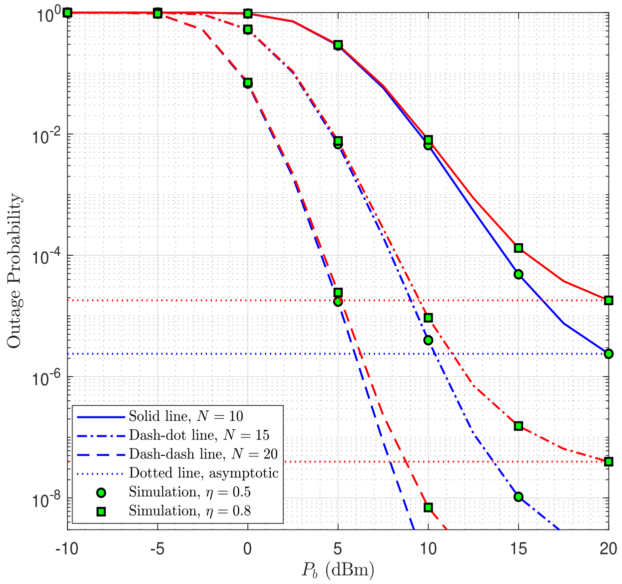

FIGURE 3. OP of primary system with optimal phase shifts in terms of the transmit power P_b.

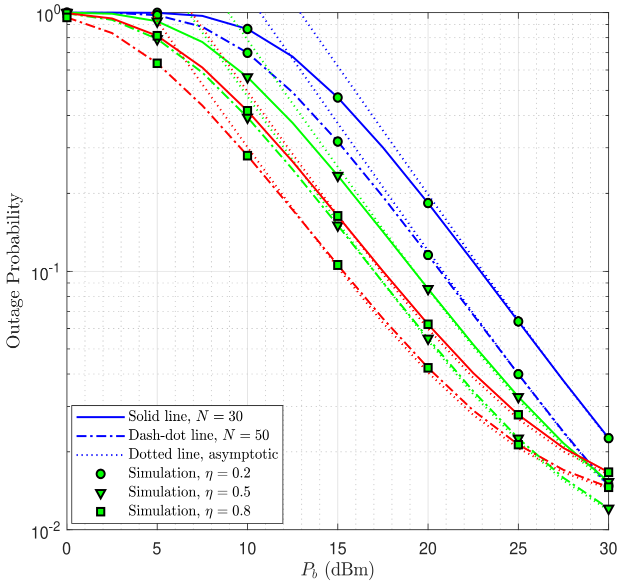

FIGURE 4. OP of backscattering secondary system in terms of the transmit power P_b.

are well-matched with the simulation results, which corroborate the theoretical analysis. Clearly, the asymptotic curves also follow the analytic curves at high P_b. It can be observed from the curves that, for the random phase shifts, increase in N does not significantly enhance the OP performance. Evidently, random phase shifting is unable to utilize the available degrees of freedom effectively. Further, a small performance improvement with N can be witnessed in low-to-medium P_b regime, whereas, for the high P_b, performance almost remains unaffected with N. Moreover, the performance is observed to be saturated at high power regime which can be attributed to the interference from the backscattering transmission. The error floor at higher P_b can also be witnessed from the flat asymptotic curves. Further, as backscattering efficiency η increases, the performance deteriorates as higher η engenders high interference to primary transmission.

In Fig. 3, we plot the outage performance of primary network in terms of the transmit power P_b for the optimal phase shift design at IRS. As can be observed, the optimal phase shift design can remarkably enhance the performance of primary system. Evidently, as N increases, the OP performance of the primary improves. However, the performance is saturated at high power regime which is also suggestive from the flat asymptotic curves. Similar to the random phase shifts case, increase in η results in degraded performance.

Fig. 4 demonstrates the OP performance of backscattering secondary system in terms of the transmit power. It can be seen from the curves that asymptotic results follow the analytic results at higher P_b, which also validates the analytical results. Evidently, with increase in N, the performance of secondary improves. Moreover, the increase in the values of η results in OP performance improvement. This is associated with the fact that a higher η provides additional power for the backscattered transmission which in turn, leads to enhanced performance. Interestingly, at higher P_b and η, the secondary performance also degrades as observed in the curves corresponding to $\eta = 0.8$ at $P_b = 30$ dB. This is due to an increased likelihood of SIC failure at higher values of η and P_b.

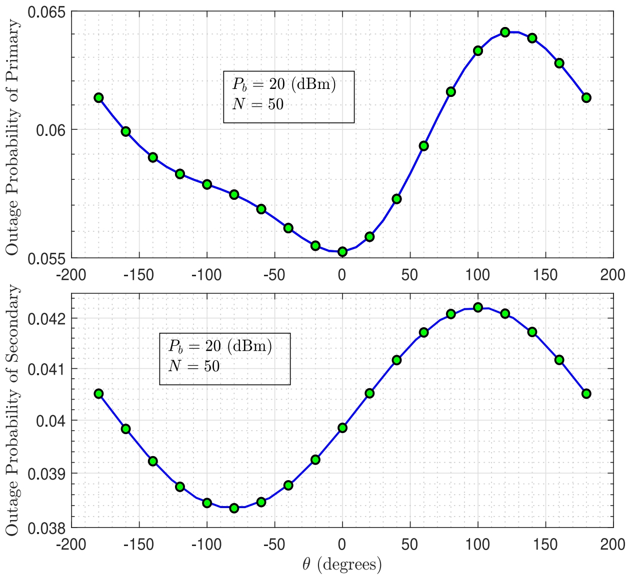

FIGURE 5. OP of primary and secondary systems in terms of the UAV's location.

In Fig. 5, we showcase the outage performance of primary system with random phase shifts and secondary backscattering system in terms of the UAV trajectory. The curves are plotted by varying the θ which governs the 3D location of UAV-IRS. Apparently, the outage probability varies as UAV

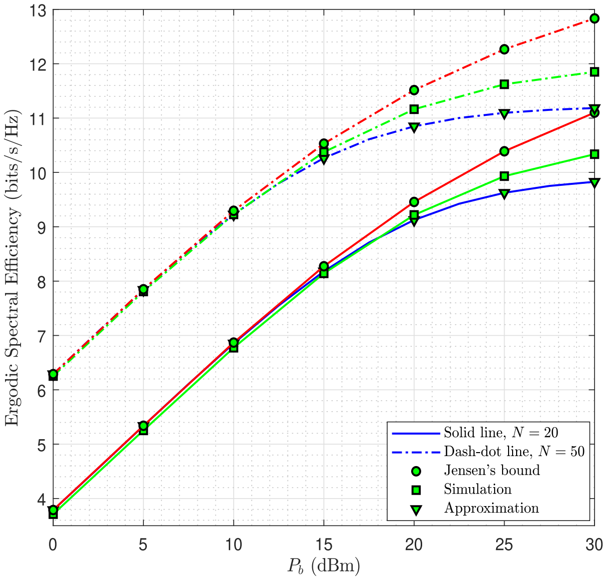

FIGURE 6. ESE of primary system with optimal phase shifts in terms of the transmit power P_b.

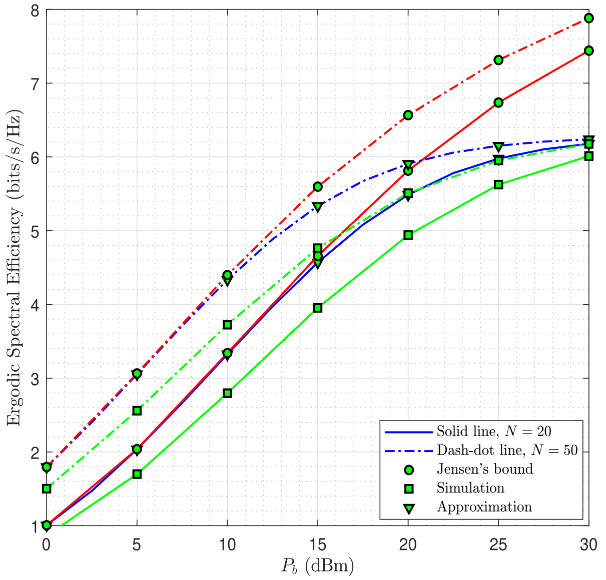

FIGURE 7. ESE of primary system with random phase shifts in terms of the transmit power P_b.

hovers around in a circular trajectory. Clearly, at certain points, the performance is found to be optimal which can be useful for the identification of proper UAV placement.

In Fig. 6, we plot the ESE performance of primary system with respect to transmit power P_b for the optimal phase shifts design to analyze the impact of N. Firstly, it can be noted that the approximation is fairly close to the exact simulation results and almost accurate in the low-to-medium transmit power regime. Further, we note from the pertinent curves that the ESE of primary system can be improved by increasing N. However, due to the interference from the backscattered transmission, the ESE of primary tends to saturate in the high transmit power regime. Similar observations can be drawn from Fig. 7 for the case of random phase shifts. Although the performance improvement in the former case is more significant than the latter with respect to varying N. Additionally, from Fig. 6 and Fig. 7, it is apparent that the gap between actual capacity (represented by simulation markers) and Jensen's bound when compared with the gap between actual capacity and obtained approximation is significantly high. This suggests that the obtained approximation is closer to the actual results than the Jensen's bound.

Fig. 8 illustrates the ESE performance of backscattering secondary system with respect to transmit power P_b. Hereby, it can be observed that increase in the number of reflective elements N results in enhanced ESE performance. Further, on comparing the curves at lower and higher P_b, it can be concluded that the ESE performance improvement with respect to N is higher at high transmit power. However, unlike the primary system, the ESE performance of secondary system does not saturate at higher P_b and monotonically improves with respect to P_b.

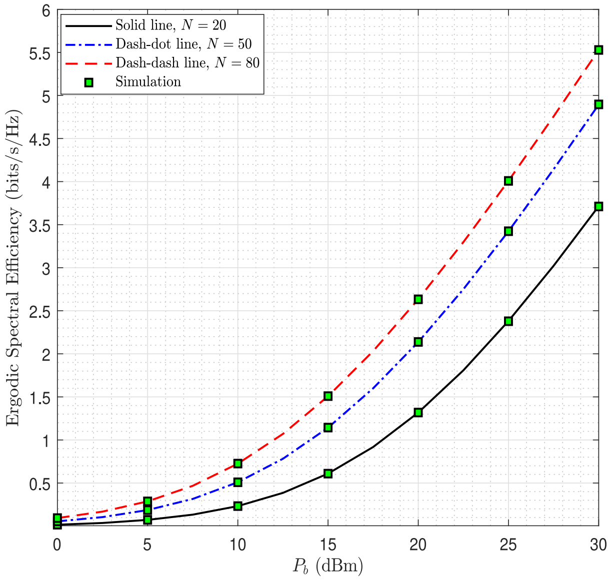

FIGURE 8. ESE of backscattering secondary system in terms of the transmit power P_b.

VI. CONCLUSION

We examined a network configuration that enabled AmBC assisted co-existence of a secondary system in aerial-IRS wireless networks. The performance is characterized by analyzing the OP and ESE. Evidently, the deployment of an UAV-IRS offers additional degrees of freedom leading to the enhanced performance for the primary system with optimal phase shifts and also for the backscattering secondary system with respect to number of reflective elements N. Primary system with random phase shifting at IRS is unable to utilize the available degrees of freedom effectively and hence

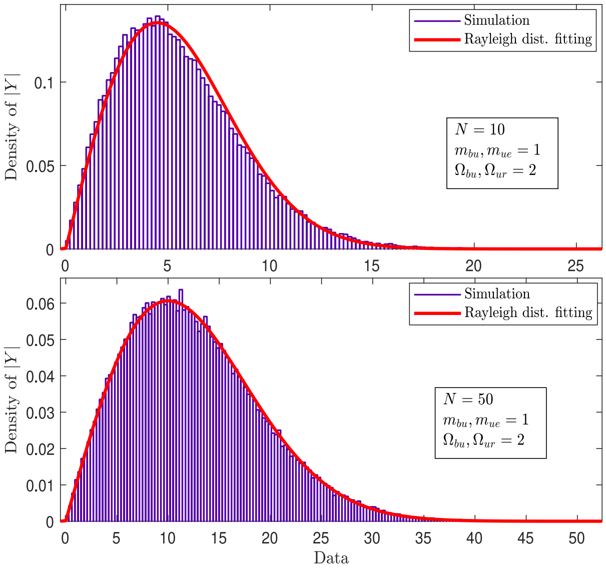

FIGURE 9. **Rayleigh approximation of $|Y|$.**

does not witness significant performance improvement with N. Also, it has been observed that backscatter efficiency is a crucial design parameter which can significantly affect the performance of both the systems. Further, it has also been noted that ESE can be improved by increasing the reflective elements of IRS. In essence, we demonstrated the feasibility of co-existence of secondary system in the primary's spectrum using AmBC technology, which can offer both spectral- and energy-efficient solutions for the future networks' deployment.

APPENDIX A
PROOF OF THEOREM 1

To evaluate the integral in (9), we first obtain the distribution of RV $Y = \mathbf{h}_{b,u}^H \boldsymbol{\Theta} \mathbf{h}_{u,r}$. Due to random phase shifts at IRS, we can write $Y = \sum_{n=1}^N |h_{b,n}||h_{n,r}|e^{j\theta_n}$ where $\theta_n = \varphi_n + \angle h_{b,n}h_{n,r}$. We express RV Y as

$$Y = \mathrm{Re}\left\{\sum_{n=1}^{N} |h_{b,n}||h_{n,r}|e^{j\theta_n}\right\} + \mathrm{Im}\left\{\sum_{n=1}^{N} |h_{b,n}||h_{n,r}|e^{j\theta_n}\right\}$$
$$= Y_n^R + Y_n^I. \tag{A.1}$$

For large N, it has been shown that Y_n^R and Y_m^I, for $n \neq m$, are independent [31], [37] and thus, by using central limit theorem, they can be represented using Gaussian distribution as

$$Y_n^R, Y_n^I \sim \mathcal{N}\left(0, \frac{N}{2}\Omega_{bu}\Omega_{ur}\right). \tag{A.2}$$

Further, due to independence between the real and imaginary parts, RV Y follows a complex Gaussian distribution. As a consequence, $|Y|$ can be characterized by a Rayleigh distribution. The accuracy of such characterization can be witnessed from the Fig. 9. As a consequence, $|Y|^2$ follows an exponential distribution [27] with PDF and CDF, respectively, as

$$f_{|Y|^2}(y) = \frac{1}{N\Omega_{bu}\Omega_{ur}} \exp\left(-\frac{y}{N\Omega_{bu}\Omega_{ur}}\right) \tag{A.3}$$

and

$$F_{|Y|^2}(y) = 1 - \exp\left(-\frac{y}{N\Omega_{bu}\Omega_{ur}}\right). \tag{A.4}$$

Following the similar lines of derivation, PDF of $|Z|^2$ can be given by

$$f_{|Z|^2}(z) = \frac{1}{N\Omega_{bu}\Omega_{ut_r}} \exp\left(-\frac{z}{N\Omega_{bu}\Omega_{ut_r}}\right). \tag{A.5}$$

Next, substituting the obtained CDF $F_Y(y)$ and PDF $f_{|Z|^2}(z)$ into (9), we can write $P_{sic}(\tau)$ as

$$P_{sic}(\tau) = \frac{1}{N\Omega_{bu}\Omega_{ut_r}} \int_{z=0}^{\infty} \exp\left(\frac{-\tau(P_b\eta\tilde{d}_3 z + \sigma_r^2)}{P_b\tilde{d}_4 N\Omega_{bu}\Omega_{ur}}\right)$$
$$\times \exp\left(-\frac{z}{N\Omega_{bu}\Omega_{ut_r}}\right)dz, \tag{A.6}$$

after solving the above integral, one can arrive at the expression in Theorem 2.

APPENDIX B
PROOF OF THEOREM 2

From the definition of OP of the primary system in (12), we have

$$P_{out}^{pri}(\mathcal{R}_p) = \Pr\left[\frac{P_b\tilde{d}_1\tilde{X}^2}{P_b\eta\tilde{d}_2|W|^2 + \sigma_e^2} \leq r_{th}^p\right]$$
$$= \int_{w=0}^{\infty} F_{\tilde{X}}\left(\sqrt{\frac{r_{th}^p(P_b\eta\tilde{d}_2 w + \sigma_e^2)}{P_b\tilde{d}_1}}\right) f_{|W|^2}(w)dw, \tag{B.1}$$

where $\tilde{X} = \sum_{n=1}^N |h_{b,n}||h_{n,e}|$. To evaluate the above integral, we first characterize the distribution of RV X using moment matching. As $h_{b,n}$ and $h_{n,e}$ follow Nakagami-m distribution, the PDF of their product ($\Xi_n = |h_{b,n}||h_{n,e}|$) can be readily obtained as [39]

$$f_{\Xi_n}(x) = \frac{4}{\Gamma(m_{bu})\Gamma(m_{ue})}\left(\frac{m_{bu}m_{ue}}{\Omega_{bu}\Omega_{ue}}\right)^{\frac{m_{bu}+m_{ue}}{2}}$$
$$\times\ x^{m_{bu}+m_{ue}-1} K_{m_{bu}-m_{ue}}\left(2x\sqrt{\frac{m_{bu}m_{ue}}{\Omega_{bu}\Omega_{ue}}}\right). \tag{B.2}$$

Next, we obtain the r-th moment $\mathbb{E}[\Xi_n(r)]$ of the RV Ξ_n as

$$\mathbb{E}[\Xi_n(r)] = \int_{x=0}^{\infty} x^r f_{\Xi_n}(x)dx, \tag{B.3}$$

on substituting PDF $f_{\Xi_n}(x)$ from (B.2) into (B.3) and thereafter solving the resultant integral using [28, eq. (6.561.16)], one can obtain

$$\mathbb{E}[\Xi_n(r)] = \left(\frac{\Omega_{bu}\Omega_{ue}}{m_{bu}m_{ue}}\right)^{\frac{r}{2}} \frac{\Gamma\left(m_{bu} + \frac{r}{2}\right)\Gamma\left(m_{ue} + \frac{r}{2}\right)}{\Gamma(m_{bu})\Gamma(m_{ue})}, \tag{B.4}$$

Based on the above, we can obtain mean and variance as

$$\mathbb{E}[\Xi_n] = \mathbb{E}[\Xi_n(1)]$$

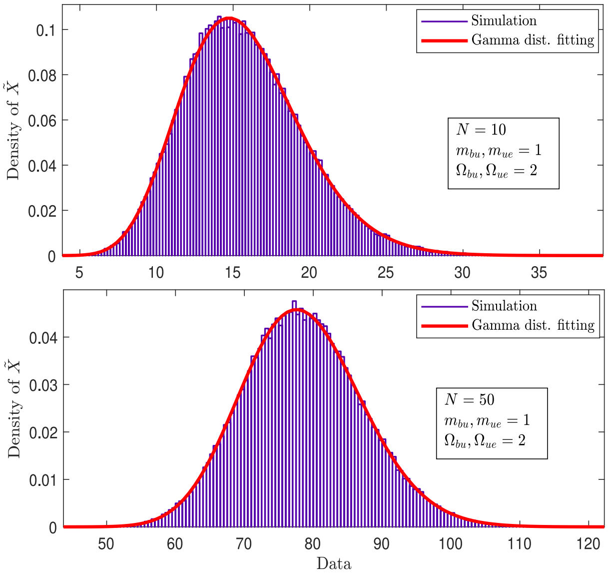

FIGURE 10. Gamma approximation of $\tilde{X}$.

$$= \left(\frac{\Omega_{bu}\Omega_{ue}}{m_{bu}m_{ue}}\right)^{\frac{1}{2}} \frac{\Gamma\left(m_{bu}+\frac{1}{2}\right)\Gamma\left(m_{ue}+\frac{1}{2}\right)}{\Gamma(m_{bu})\Gamma(m_{ue})} \tag{B.5}$$

$$\begin{aligned} \text{and } \mathrm{Var}[\Xi_n] &= \mathbb{E}[\Xi_n(2)] - (\mathbb{E}[\Xi_n])^2 \\ &= \Omega_{bu}\Omega_{ue} - (\mathbb{E}[\Xi_n])^2. \end{aligned} \tag{B.6}$$

Finally, we can match the distribution of $\tilde{X} = \sum_{n=1}^{N} \Xi_n$ to a Gamma distribution with the following shape k_x and scale β_x parameters

$$k_x = N\frac{(\mathbb{E}[\Xi_n])^2}{\mathrm{Var}[\Xi_n]} \text{ and } \beta_x = \frac{\mathrm{Var}[\Xi_n]}{\mathbb{E}[\Xi_n]}. \tag{B.7}$$

The accuracy of this characterization can be witnessed from the Fig. 10. Next, using the obtained parameters in (B.7), the CDF of a Gamma distributed RV $\tilde{X}$ can be given by [40]

$$F_{\tilde{X}}(x) = \frac{1}{\Gamma(k_x)}\Upsilon\left(k_x, \frac{x}{\beta_x}\right), \tag{B.8}$$

which can be expressed using a series representation of incomplete Gamma function [41] as

$$F_{\tilde{X}}(x) = \sum_{n=0}^{L} \frac{1}{\Gamma(k_x+n+1)\beta_x^{k_x+n}} x^{k_x+n} \exp\left(-\frac{x}{\beta_x}\right). \tag{B.9}$$

Hereby, L equals infinity provides exact values of $F_{\tilde{X}}(x)$, however, even for $L = 20$, the series converges to sufficient level of accuracy. Further, following the approach in Appendix A, we obtain PDF of $|W|^2$ as

$$f_{|W|^2}(w) = \frac{1}{N\Omega_{bu}\Omega_{ut_e}} \exp\left(-\frac{w}{N\Omega_{bu}\Omega_{ut_e}}\right). \tag{B.10}$$

On substituting (B.9) and (B.10) in (B.1) and followed by appropriate substitutions, we have

$$\begin{aligned} P_{out}^{pri}(\mathcal{R}_p) = {} & \sum_{n=0}^{L} \exp\left(\frac{\sigma_e^2}{P_b N\Omega_{bu}\Omega_{ut_e}\eta\tilde{d}_2}\right)\frac{2}{\Gamma(k_x+n+1)} \\ & \times \frac{1}{N\Omega_{bu}\Omega_{ut_e}} \frac{\tilde{d}_1\beta_x^2}{r_{th}^p\eta\tilde{d}_2} \int_{v=\sqrt{\frac{r_{th}^p\sigma_e^2}{P_b\tilde{d}_1\beta_x^2}}}^{\infty} v^{k_x+n+1} \\ & \times \exp\left(-v - \frac{\tilde{d}_1\beta_x^2 v^2}{r_{th}^p\eta\tilde{d}_2 N\Omega_{bu}\Omega_{ut_e}}\right)dv. \end{aligned} \tag{B.11}$$

For simplification, let us denote the integral in (B.11) by $\mathcal{A}(\mathcal{R}_p)$. Apparently, the integral $\mathcal{A}(\mathcal{R}_p)$ is intricate to evaluate for the closed-form solution, however, it can be analyzed using the numerical methods or any computing software.

APPENDIX C
PROOF OF COROLLARY 1

Using (12) and (B.1), we can express $P_{out}^{pri}(\mathcal{R}_p)$ at asymptotic limit $P_b \to \infty$ as

$$P_{out}^{pri}(\mathcal{R}_p) \underset{P_b\to\infty}{\simeq} \int_{w=0}^{\infty} F_{\tilde{X}}\left(\sqrt{\frac{r_{th}^p\eta\tilde{d}_2 w}{\tilde{d}_1}}\right) f_{|W|^2}(w)dw, \tag{C.1}$$

on invoking CDF $F_{\tilde{X}}(\cdot)$ from (B.9) and PDF $f_W(w)$ from (B.10) into (C.1) followed by variable transformation and substitution, we can express

$$\begin{aligned} P_{out}^{pri}(\mathcal{R}_p) \underset{P_b\to\infty}{\simeq} {} & \sum_{n=0}^{L} \frac{2}{\Gamma(k_x+n+1)} \frac{\tilde{d}_1\beta_x^2}{r_{th}^p\eta\tilde{d}_2} \frac{1}{N\Omega_{bu}\Omega_{ut_e}} \\ & \times \int_{t=0}^{\infty} t^{k_x+n+1} \exp\left(-t - \frac{\beta_x^2\tilde{d}_1 t^2}{r_{th}^p\eta\tilde{d}_2 N\Omega_{bu}\Omega_{ut_e}}\right)dt, \end{aligned} \tag{C.2}$$

on solving the above integral using [28, eq. (3.462)], we can obtain the expression as given in Corollary 1.

APPENDIX D
PROOF OF THEOREM 3

To derive the OP of primary system with random phase shifts, we can express (17) in an integral form as

$$P_{out,rp}^{pri}(\mathcal{R}_p) = \int_{w=0}^{\infty} F_{|X|^2}\left(\frac{r_{th}^p}{P_b\tilde{d}_1}(P_b\eta\tilde{d}_2 w + \sigma_e^2)\right) f_{|W|^2}(w)dw. \tag{D.1}$$

Owing to random phase shifts at IRS, the RV X can be written as $X = \mathbf{h}_{b,u}^H\mathbf{\Theta}\mathbf{h}_{u,e} = \sum_{n=1}^{N} |h_{b,n}||h_{n,e}|e^{j\theta_n}$, where $\theta_n = \varphi_n + \angle h_{b,n}h_{n,e}$. Following the reasoning in Appendix A, it can be shown that the amplitude of complex RV X can be characterized by a Rayleigh distribution and thereby $|X|^2$ follows an exponential distribution with its PDF and CDF given, respectively, by

$$f_{|X|^2}(x) = \frac{1}{N\Omega_{bu}\Omega_{ue}} \exp\left(-\frac{x}{N\Omega_{bu}\Omega_{ue}}\right) \tag{D.2}$$

and

$$F_{|X|^2}(x) = 1 - \exp\left(-\frac{x}{N\Omega_{bu}\Omega_{ue}}\right). \tag{D.3}$$

On invoking $F_{|X|^2}(x)$ from (D.3) and $f_{|W|^2}(w)$ from (B.10) into (D.1) and subsequently evaluating the resultant integral leads to expression of $P_{out,rp}^{pri}(\mathcal{R}_p)$ in Theorem 3.

APPENDIX E
PROOF OF COROLLARY 3

To derive OP in Corollary 3, we first obtain $P_{sic}^{asy}(\tau)$ using (9) at $P_b \to \infty$ as

$$P_{sic}^{asy}(\tau) \underset{P_b\to\infty}{\simeq} 1 - \int_{z=0}^{\infty} F_{|Y|^2}\left(\frac{\tau\eta\tilde{d}_3 z}{\tilde{d}_4}\right) f_{|Z|^2}(z)dz, \tag{E.1}$$

which, after substituting the respective CDF and PDF, can be expressed as

$$P_{sic}^{asy}(\tau) \underset{P_b\to\infty}{\simeq} \frac{1}{N\Omega_{bu}\Omega_{ut_r}} \int_{z=0}^{\infty} \exp\left(\frac{-\tau\eta\tilde{d}_3 z}{\tilde{d}_4 N\Omega_{bu}\Omega_{ur}}\right) \times \exp\left(-\frac{z}{N\Omega_{bu}\Omega_{ut_r}}\right)dz, \tag{E.2}$$

on computing the above integral, (24) can be obtained. Further, utilizing the approximation $\exp(-x) \underset{x\to 0}{\simeq} 1-x$, along with obtained $\bar{P}_{sic}^{asy}(\tau)$ into (23), Corollary 3 is proved.

APPENDIX F
DERIVATION OF (28) AND (29)

To derive $\mathbb{E}[|\tilde{X}|^2]$, we use the transformation of a RV $V = |\tilde{X}|^2$ as follows

$$F_{|\tilde{X}|^2}(x) = F_{\tilde{X}}(\sqrt{x}), \quad x > 0, \tag{F.1}$$

based on the above relationship, the PDF of $|\tilde{X}|^2$ can be expressed as

$$f_{|\tilde{X}|^2}(x) = f_V(x) = \frac{1}{2\sqrt{x}} f_{\tilde{X}}(\sqrt{x}). \tag{F.2}$$

Utilizing this PDF, we can further obtain $\mathbb{E}[|X|^2]$ as

$$\mathbb{E}\left[|\tilde{X}|^2\right] = \int_0^\infty v f_V(v)dv = \int_0^\infty \frac{\sqrt{v}}{2} f_{\tilde{X}}\left(\sqrt{v}\right)dv. \tag{F.3}$$

From Appendix B, we can deduce

$$f_{\tilde{X}}(x) = \frac{1}{\Gamma(k_x)\beta_x^{k_x}} x^{k_x - 1} \exp\left(-\frac{x}{\beta_x}\right), \tag{F.4}$$

on invoking (F.4) into (F.3) followed by subsequent evaluation of the resultant integral yields (28). Further, in Appendix B, it is observed that $|W|^2$ can be characterized by an exponential distribution with its PDF in (B.10). Therefore, $\mathbb{E}[|W|^2]$ can be readily obtained as given by (29).

APPENDIX G
DERIVATION OF (33)

To derive (33), we first use the following transformation

$$\mathbb{E}\left[\log_2(1+\zeta)\right] = \log_2(e) \int_0^\infty \frac{1 - F_\zeta(z)}{1+z} dz, \tag{G.1}$$

where $\zeta = \frac{P_b}{\sigma_r^2}\eta\tilde{d}_3|\mathbf{h}_{b,u}^H\boldsymbol{\Theta}\mathbf{h}_{u,t_r}|^2 = \frac{P_b}{\sigma_r^2}\eta\tilde{d}_3|Z|^2$ and $F_\zeta(\cdot)$ is its CDF. Based on (A.5) in Appendix A, we can obtain CDF of ζ as

$$F_\zeta(z) = 1 - \exp\left(\frac{-z\sigma_r^2}{P_b\eta\tilde{d}_3 N\Omega_{bu}\Omega_{ut_r}}\right). \tag{G.2}$$

Invoking (G.1) and (G.2) in (32) and eventually computing the resultant integral with the aid of [28, eq. (3.352.4)], the expression in (33) can be obtained.

REFERENCES

[1] M. Di Renzo *et al.*, "Reconfigurable intelligent surfaces vs. relaying: Differences, similarities, and performance comparison," *IEEE Open J. Commun. Soc.*, vol. 1, pp. 798–807, 2020.

[2] M. Najafi, V. Jamali, R. Schober, and H. V. Poor, "Physics-based modeling and scalable optimization of large intelligent reflecting surfaces," *IEEE Trans. Commun. Soc.*, vol. 69, no. 4, pp. 2673–2691, Apr. 2021.

[3] M. M. Azari *et al.*, "Evolution of non-terrestrial networks from 5G to 6G: A survey," Jul. 2021, *arXiv:2107.06881*.

[4] P. S. Bithas, V. Nikolaidis, A. G. Kanatas, and G. K. Karagiannidis, "UAV-to-ground communications: Channel modeling and UAV selection," *IEEE Trans. Commun.*, vol. 68, no. 8, pp. 5135–5144, Aug. 2020.

[5] M. M. Azari, S. Solanki, S. Chatzinotas, and M. Bennis, "THz-empowered UAVs in 6G: Opportunities, challenges, and trade-offs," Jan. 2022, *arXiv:2201.07886*.

[6] Q. Wu *et al.*, "A comprehensive overview on 5G-and-beyond networks with UAVs: From communications to sensing and intelligence," *IEEE J. Sel. Areas Commun.*, vol. 39, no. 10, pp. 2912–2945, Oct. 2021.

[7] Q. Zhang, W. Saad, and M. Bennis, "Reflections in the sky: Millimeter wave communication with UAV-carried intelligent reflectors," in *Proc. IEEE Globecom*, Waikoloa, HI, USA, Dec. 2019, pp. 1–6.

[8] T. Shafique, H. Tabassum, and E. Hossain, "Optimization of wireless relaying with flexible UAV-borne reflecting surfaces," *IEEE Trans. Commun.*, vol. 69, no. 1, pp. 309–325, Jan. 2021.

[9] H. Lu, Y. Zeng, S. Jin, and R. Zhang, "Aerial intelligent reflecting surface: Joint placement and passive beamforming design with 3D beam flattening," *IEEE Trans. Wireless Commun.*, vol. 20, no. 7, pp. 4128–4143, Jul. 2021.

[10] X. Tang, D. Wang, R. Zhang, Z. Chu, and Z. Han, "Jamming mitigation via aerial reconfigurable intelligent surface: Passive beamforming and deployment optimization," *IEEE Trans. Veh. Technol.*, vol. 70, no. 6, pp. 6232–6237, Jun. 2021.

[11] A. Mahmoud, S. Muhaidat, P. C. Sofotasios, I. Abualhaol, O. A. Dobre, and H. Yanikomeroglu, "Intelligent reflecting surfaces assisted UAV communications for IoT networks: Performance analysis," *IEEE Trans. Green Commun. Netw.*, vol. 5, no. 3, pp. 1029–1040, Sep. 2021.

[12] N. Gao, S. Jin, X. Li, and M. Matthaiou, "Aerial RIS-assisted high altitude platform communications," *IEEE Wireless Commun. Lett.*, vol. 10, no. 10, pp. 2096–2100, Oct. 2021.

[13] N. V. Huynh, D. T. Hoang, X. Lu, D. Niyato, P. Wang, and D. I. Kim, "Ambient backscatter communications: A contemporary survey," *IEEE Commun. Surveys Tuts.*, vol. 20, no. 4, pp. 2889–2922, 4th Quart., 2018.

[14] S. Gautam, S. Solanki, S. K. Sharma, S. Chatzinotas, and B. Ottersten, "Hybrid active-and-passive relaying model for 6G-IoT greencom networks with SWIPT," *Sensors*, vol. 21, no. 18, p. 6013, Sep. 2021.

[15] X. Kang, Y.-C. Liang, and J. Yang, "Riding on the primary: A new spectrum sharing paradigm for wireless-powered IoT devices," *IEEE Trans. Wireless Commun.*, vol. 17, no. 9, pp. 6335–6347, Sep. 2018.

[16] H. Guo, R. Long, and Y.-C. Liang, “Cognitive backscatter network: A spectrum sharing paradigm for passive IoT,” *IEEE Commun. Lett.*, vol. 8, no. 5, pp. 1423–1426, Oct. 2019.

[17] H. Guo, Y.-C. Liang, R. Long, and Q. Zhang “Cooperative ambient backscatter system: A symbiotic Radio paradigm for passive IoT,” *IEEE Wireless Commun. Lett.*, vol. 8, no. 4, pp. 1191–1194, Aug. 2019.

[18] H. Ding, D. B. da Costa, and J. Ge, “Outage analysis for cooperative ambient backscatter systems,” *IEEE Wireless Commun. Lett.*, vol. 9, no. 5, pp. 601–605, May 2020.

[19] W. Zhao, G. Wang, S. Atapattu, T. A. Tsiftsis, and X. Ma, “Performance analysis of large intelligent surface aided backscatter communication systems,” *IEEE Wireless Commun. Lett.*, vol. 9, no. 7, pp. 962–966, Jul. 2020.

[20] H. Chen, G. Yang, and Y.-C. Liang, “Joint active and passive beamforming for reconfigurable intelligent surface enhanced symbiotic radio system,” *IEEE Wireless Commun. Lett.*, vol. 10, no. 5, pp. 1056–1060, May 2021.

[21] J. Zuo, Y. Liu, L. Yang, L. Song, and Y.-C. Liang, “Reconfigurable intelligent surface enhanced NOMA assisted backscatter communication system,” *IEEE Trans. Veh. Technol.*, vol. 70, no. 7, pp. 7261–7266, Jul. 2021.

[22] Z. Yang, L. Feng, F. Zhou, X. Qiu, and W. Li, “Analytical performance analysis of intelligent reflecting surface aided ambient backscatter communication network,” *IEEE Wireless Commun. Lett.*, vol. 10, no. 12, pp. 2732–2736, Dec. 2021.

[23] X. Jia and Z. Zhou, “IRS-assisted ambient backscatter communications utilizing deep reinforcement learning,” *IEEE Wireless Commun. Lett.*, vol. 10, no. 11, pp. 2374–2378, Nov. 2021.

[24] C. Liaskos, A. Tsioliaridou, S. Ioannidis, A. Pitsillides, and I. F. Akyildiz, “Realizing ambient backscatter communications with intelligent surfaces in 6G wireless systems,” *IEEE Wireless Commun.*, early access, Nov. 16, 2021, doi: 10.1109/MWC.101.2100233.

[25] S. Solanki, S. Gautam, V. Singh, S. K. Sharma, and S. Chatzinotas, “Symbiotic radio based spectrum sharing in cooperative UAV-IRS wireless networks,” in *Proc. VTC-Spring*, Mar. 2022, pp. 1–5.

[26] S. Solanki, P. K. Upadhyay, D. B. da Costa, P. S. Bithas, and A. G. Kanatas, “Performance analysis of cognitive relay networks with RF hardware impairments and CEEs in the presence of primary users’ interference,” *IEEE Trans. Cogn. Commun. Netw.*, vol. 4, no. 2, pp. 406–421, Jun. 2018.

[27] S. Solanki, P. K. Upadhyay, D. B. Da Costa, H. Ding, and J. M. Moualeu, “Performance analysis of piece-wise linear model of energy harvesting-based multiuser overlay spectrum sharing networks,” *IEEE Open J. Commun. Soc.*, vol. 1, pp. 1820–1836, 2020.

[28] I. S. Gradshteyn and I. M. Ryzhik, *Tables of Integrals, Series and Products*, 7th ed. New York, NY, USA: Academic, 2007.

[29] Q. Tao, J. Wang, and C. Zhong, “Performance analysis of intelligent reflecting surface aided communication systems,” *IEEE Commun. Lett.*, vol. 24, no. 11, pp. 2464–2468, Nov. 2020.

[30] A. Al-Hourani, S. Kandeepan, and S. Lardner, “Optimal LAP altitude for maximum coverage,” *IEEE Wireless Commun. Lett.*, vol. 3, no. 6, pp. 569–572, Dec. 2014.

[31] D. Selimis, K. P. Peppas, G. C. Alexandropoulos, and F. I. Lazarakis, “On the performance analysis of RIS-empowered communications over Nakagami-*m* fading,” *IEEE Commun. Lett.*, vol. 25, no. 7, pp. 2191–2195, Jul. 2021.

[32] U. Singh, S. Solanki, D. S. Gurjar, P. K. Upadhyay, and D. B. da Costa, “Wireless power transfer in two-way AF relaying with maximal-ratio combining under Nakagami-m fading,” in *Proc. Int. Wireless Commun. Mobile Comput. Conf. (IWCMC)*, Limassol, Cyprus, Aug. 2018, pp. 169–173.

[33] Q. Wu and R. Zhang, “Intelligent reflecting surface enhanced wireless network via joint active and passive beamforming,” *IEEE Trans. Wireless Commun.*, vol. 18, no. 11, pp. 5394–5409, Aug. 2019.

[34] M. Di Renzo *et al.*, “Smart radio environments empowered by reconfigurable intelligent surfaces: How it works, state of research, and the road ahead,” *IEEE J. Sel. Areas Commun.*, vol. 38, no. 11, pp. 2450–2525, Nov. 2020.

[35] A. Zappone, M. Di Renzo, F. Shams, X. Qian, and M. Debbah, “Overhead-aware design of reconfigurable intelligent surfaces in smart radio environments,” *IEEE Trans. Wireless Commun.*, vol. 20, no. 1, pp. 126–141, Jan. 2021.

[36] L. Yang, F. Meng, J. Zhang, M. O. Hasna, and M. D. Renzo, “On the performance of RIS-assisted dual-hop UAV communication systems,” *IEEE Trans. Veh. Technol.*, vol. 69, no. 9, pp. 10385–10390, Sep. 2020.

[37] B. Tahir, S. Schwarz, and M. Rupp, “Analysis of uplink IRS-assisted NOMA under Nakagami-*m* fading via moments matching,” *IEEE Wireless Commun. Lett.*, vol. 10, no. 3, pp. 624–628, Mar. 2021.

[38] S. A. Tegos, D. Tyrovolas, P. D. Diamantoulakis, C. K. Liaskos, and G. K. Karagiannidis, “On the distribution of the sum of double-Nakagami-*m* random vectors and application in randomly reconfigurable surfaces,” Feb. 2021, *arXiv:2102.05591*.

[39] R. C. Ferreira, M. S. P. Facina, F. A. P. De Figueiredo, G. Fraidenraich, and E. R. De Lima, “Bit error probability for large intelligent surfaces under double-Nakagami fading channels,” *IEEE Open J. Commun. Soc.*, vol. 1, pp. 750–759, 2020.

[40] S. Solanki, D. S. Gurjar, P. K. Sharma, S. K. Sharma, and S. Chatzinotas, “On the secrecy-reliability performance trade-off for NOMA-enabled 5G mmWave networks,” in *Proc. IEEE PIMRC*, Helsinki, Finland, Sep. 2021, pp. 720–725.

[41] S. Solanki, P. K. Sharma, and P. K. Upadhyay, “Adaptive link utilization in two-way spectrum sharing relay systems under average interference-constraints,” *IEEE Syst. J.*, vol. 12, no. 4, pp. 3461–3472, Dec. 2018.

SOURABH SOLANKI (Member, IEEE) received the M.Tech. degree in communication and signal processing and the Ph.D. degree in electrical engineering from the Indian Institute of Technology—Indore, India, in 2015 and 2019, respectively. From 2019 to 2020, he was a Research Professor with Korea University, Seoul, South Korea, where he received the Brain Korea 21 Postdoctoral Fellowship by the National Research Foundation, Government of Korea. Since 2021, he has been working as a Research Associate with the Interdisciplinary Center for Security, Reliability and Trust (SnT), University of Luxembourg, Luxembourg. His main research interests include cognitive radio, terahertz communications, mmWave networks, energy harvesting, and non-terrestrial networks. He received the Exemplary Reviewer Award for IEEE TRANSACTIONS ON COMMUNICATIONS in 2020. He was a co-recipient of the Best Paper Award with the International Conference on ICT Convergence, Jeju Island, South Korea, in October 2020. He has been serving as a technical program committee member of various conferences and has also been involved in peer review process of major IEEE journals and conferences.

SUMIT GAUTAM (Member, IEEE) received the B.Tech. degree (Hons.) in electronics and communication engineering from the LNM Institute of Information Technology (Deemed University), Jaipur, India, in 2013, the M.S. degree in electronics and communication engineering by research from the International Institute of Information Technology Hyderabad (Deemed University), Hyderabad, India, in 2017, and the Ph.D. degree in computer science (with focus on wireless communications) from the Interdisciplinary Centre for Security, Reliability, and Trust (SnT), University of Luxembourg, Luxembourg, in 2020. Since December 2021, he has been working as an Assistant Professor with the Indian Institute of Technology—Indore, India. Prior to this, he worked as a Consultant: BTS Algorithm and Channel Modeling Expert with Incluso AB (Client: Huawei Technologies Sweden AB), Gothenburg, Sweden, from August 2021 to December 2021. He was a Research Associate/Postdoctoral Researcher with SnT, University of Luxembourg from March 2020 to July 2021. His research interests include simultaneous wireless information and power transfer, caching, optimization methods, hybrid active-and-passive cooperative communications, and precoding for multi-group multicast systems.

SHREE KRISHNA SHARMA (Senior Member, IEEE) received the Ph.D. degree in wireless communications from the University of Luxembourg in 2014. He held various research and academic positions with SnT, University of Luxembourg; Western University, Canada; and Ryerson University, Canada. He has published more than 100 technical papers in scholarly journals, international conferences, and book chapters, and has over 4400 google scholar citations with an h-index of 30. He is a Lead Editor of two IET books on *Satellite Communications in the 5G Era* and *Communications Technologies for Networked Smart Cities*.

SYMEON CHATZINOTAS (Senior Member, IEEE) is currently a Full Professor and the Head of the SIGCOM Research Group with SnT, University of Luxembourg. He coordinates research activities in communications and networking, acting as a PI in over 40 projects and is the main representative for 3GPP, ETSI, DVB. In the past, he worked as a Visiting Professor with the University of Parma, Italy, lecturing on 5G Wireless Networks. He was involved in numerous R&D Projects for NCSR Demokritos, CERTH Hellas and CCSR, University of Surrey. He was a co-recipient of the 2014 IEEE Distinguished Contributions to Satellite Communications Award and Best Paper Awards at 5GWF, EURASIP JWCN, CROWNCOM, and ICSSC. He has (co-)authored more than 600 technical papers in refereed international journals, conferences, and scientific books. He is currently on the Editorial Board of the IEEE TRANSACTIONS ON COMMUNICATIONS, IEEE OPEN JOURNAL OF VEHICULAR TECHNOLOGY, and the *International Journal of Satellite Communications and Networking*.